[1] **Pawan Kumar Sharma**

[2] **Eakagra Galav**

[3] **Dharm Veer Arya**

[4] **Anuj Baliyan**

Instability Analysis with Mitigation Strategies in Ocean and Agro-Industrial Products for Sustainability

JES

Journal of Electrical Systems

Abstract: - The ever-increasing instability challenges posed by climate change, energy sustainability and environmental conservation have brought about a critical need for an in-depth study and analysis of ionospheric disturbance due to natural disasters such as tsunami and instability mitigation by sugarcane-lithium products in crude oil. Computational results of instability for area, production and yield have revealed that sugarcane exhibits low instability across the world, thus making it an attractive option. Despite high instability during the session (2008-09 to 2010-11) and after 2017-18 in net profit of sugar import-export in India, the country has shown significant economic growth during the COVID-19 pandemic. Moreover, the reduction in cost of Li-ion batteries has made electric vehicles and renewable energy systems more affordable, thereby increasing their demand. Additionally, a detailed analysis of TIM devices for energy conservation shows that a honeycomb cell with an aspect ratio of 2 to 13 is sufficient to suppress instability in the air layer for inclination up to 90^0 and ΔT from 20^0 to 120^0. Overall, these findings suggest that sugarcane-lithium products and TIM devices can play a crucial role in mitigating instability challenges in climate change, energy sustainability and environmental conservation.

Keywords: Instability, Mitigation, Tsunami, Honeycomb Devices, Li-ion Battery.

Nomenclature					
Cuddy Della- Valle Index	$CDVI$	Hot surface temperature	T_h	Wave number	h
Coefficient of variation	CV	Cold surface temperature	T_c	Density	ρ
Coefficient of determination	R^2	Temperature difference	ΔT	Angle with x-axis	δ
Coefficient of volume expansion	α	Temperature at time t_0	T_0	Laplacian operator	∇^2
Transparent Insulation Material	TIM	Mean temperature	T_m	There exists	$\exists$
Depth of cellular structure	L	Gravity constant	g	Vorticity vector	ω
Width of cellular structure	d	Nusselt number	N_u	Standard deviation	σ
Absorptance-transmittance product	$(\alpha\tau)_{eff}$	Prandtl number	P_r	Thermal diffusivity	κ
Overall heat transfer coeff. for TIM	U_L	Atmospheric pressure	p	Effectiveness	ε
Perturbation in temperature	θ	Aspect ratio	A	Kinetic viscosity	ν
Minimum horizontal speed of Tsunami	$(U_x)_{min}$	Random variable	X	Angle of inclination	β
Maximum horizontal speed of Tsunami	$(U_x)_{max}$	Mean	$\bar{X}$	Number of variables	n
Critical Rayleigh number	R_c	Rayleigh number	R_a	Gigawatt-hour	GWh

I. INTRODUCTION

Instability is a generator of opportunities in each field of ocean, agriculture, industry and buildings. In this regard, we are focusing to evaluate the following:

A. Ionospheric disturbance due to tsunami   B. Instability analysis in food grains, ethanol, sugarcane and sugar C. Mitigation of oil crisis by sugarcane, ethanol and lithium   D. Instability analysis in fluids for horizontal and inclined planes   E. Instability mitigation in fluid bounded by honeycomb structures.

A. *Ionospheric Disturbance due to Tsunami*

Tsunamis, triggered by underwater seismic activities like earthquakes, volcanic eruptions, or landslides, pose significant threats through widespreasd flooding, infrastructure damage, and loss of life. This study examines the characteristics of tsunamis and their associated travelling ionospheric disturbances (TID). The speed disparity between tsunamis and TIDs arises from wave propagation mechanisms. For instance, the Sumatra-Andaman tsunami on December 26, 2004, recorded an average speed of 804 km/h in the open ocean, while the average speed of TID displacement was 670 km/h. The travel speed of a typical tsunami, with a wave period oscillation of 18 minutes, exhibits a period length $T = \frac{\lambda}{v}$ ranging from 15 to 60 minutes. Based on Arya's work [1], the speed of a tsunami wave depends on the ocean's depth, adhering to the equation $v = \sqrt{gh}$, which spans a range of 36 to 720 km/h. Computed travel speeds for tsunami wave periods of 15, 18, 20, and 25 minutes are presented in Fig. 1. This research aims to enhance our understanding of tsunamis, their impacts and the dynamics governing their wave propagation.

[1] * Corresponding author

[1, 2, 3, 4] Department of Mathematics, Bareilly College Bareilly, Uttar Pradesh, India, 243005

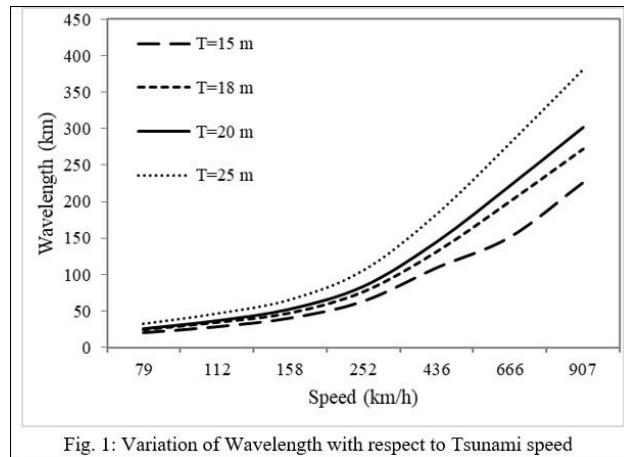*pksharma1170@gmail.com, eakagrav98@gmail.com, dvarya1857@gmail.com, anujbaliyan0405@gmail.com*

Fig. 1: Variation of Wavelength with respect to Tsunami speed

In various research articles, the concept we are discussing has been extensively explored. Koustov and Schlegel [2] conducted a comprehensive analysis of the properties and behavior of internal gravity waves within the atmosphere. Fukushima *et al* [3] and Moum *et al* [4] investigated the utilization of a fully nonlinear Boussinesq model to simulate tsunami propagation. They highlighted how internal waves can impact the density structure of the ocean, resulting in the mixing and transportation of nutrients and other materials. Synolakis [5] described how tsunami waves in the deep waters of the open ocean exhibit small amplitudes and are often imperceptible at sea. However, as they approach shallower water near the coast, their speed decreases while their height increases substantially, reaching tens of meters. Synolakis and Skgelbreia [6] further explained that when tsunamis reach the shore, there is a transfer of energy into the wave spectrum, manifesting as a series of breaking waves. In brief, the disturbance caused by tsunami in the atmosphere can be considered as a perturbation in the stationary, stratified atmosphere that is affected by a gravitational field (0, 0, -g) in vertical z-direction. The perturbations, traveling with a velocity of u, induce fluctuations ρ' and p' in the gas density (ρ_0) and pressure (p_0) respectively, resulting in additional forces ($\rho' g$ and - grad p') that counterbalance the internal forces $p(du/dt)$ and induce oscillations. These oscillations are governed by the equation of state and the equation of mass conservation for gas. The disturbed motion is bounded at the bottom by the tsunami profile, which is assumed to be deformed according to a given function   z' = F (x, y, t). The disturbed motion must comply with the free boundary condition at infinity, where the energy of the perturbation becomes zero. To calculate the energy transferred to internal atmospheric gravity waves by the motion of the tsunami through the atmosphere, it is necessary to determine the solution for internal waves that satisfy the aforementioned boundary conditions of the disturbed motion. Following Kaushika [7-8], the tsunami can be seen like a little mountain moving with velocity v and assuming it as an infinite extent along y-direction, then its profile can be represented by

$$\text{z' = Re} \int_0^\infty A(k) e^{ik(vt-x)} dk \tag{1}$$

with boundary condition at z = 0. Corresponding to this profile, internal atmospheric wave solution given by Huies [9] will yield the density fluctuation ρ' represented as

$$\frac{\rho'}{p_0} = \frac{(\gamma-1)^{1/2}}{c} \cdot \frac{vc^2}{(v^2-c^2)} \cdot e^{\lambda g^2/2c^2} \cdot \frac{ab}{(a^2+x^2)^{1/2}} (l^2 + m^2)^{1/2} \left(\frac{e^{-ak_1} + e^{-ak_2}}{e^{-ak_1} - e^{-ak_2}} \right)_{min}^{max} \tag{2}$$

where p_0 is the ambient pressure, γ is the adiabatic index, c is the speed of sound, λ is the wavelength of the tsunami, g is the acceleration due to gravity, a and b are constants, x is the position along the x-axis, l and m are wave numbers.

Consider a tsunami with a height of 8 m, velocity of 100 m/s, horizontal extent of 20 km, and wavelength of 150 km. The permissible internal gravity wave modes at ionospheric heights have wave numbers ranging from 10^{-6} to 10^{-8} cm^{-1}. In this range, the wave satisfies a simplified dispersion relation $m = \frac{\omega}{v}$ and falls within the range of k = 10^{-6} through 10^{-8} cm^{-1}. The symbol ω represents the angular frequency of the wave and ν represents the phase velocity of the wave. e^{-ak_1} and e^{-ak_2} describe how certain quantities decay or attenuate as they interact with internal atmospheric waves, providing insights into the behavior and impact of these waves on the considered scenario. The values for e^{-ak_1} and e^{-ak_2} may be taken as 0.37 and 0.99 respectively. The given prompt describes the representation of a tsunami's profile and the corresponding density fluctuation caused by internal atmospheric waves. In this way we will get minimum and maximum values of U_x, representing the horizontal speed of the tsunami, for different values of a as represented in Table 1 and Fig. 2 represents the minimum and maximum density fluctuation with respect to horizontal speed of tsunami.

Table 1: Density fluctuation for horizontal speed of tsunami				
X	$(U_x)_{min}$ (km/h)	$\left(\frac{\rho'}{p_0}\right)_{min}$	$(U_x)_{max}$ (km/h)	$\left(\frac{\rho'}{p_0}\right)_{max}$
$10a$	270	0.155	540	0.31
$20a$	133	0.077	270	0.155
$50a$	54	0.031	108	0.062
$100a$	27	0.015	54	0.031
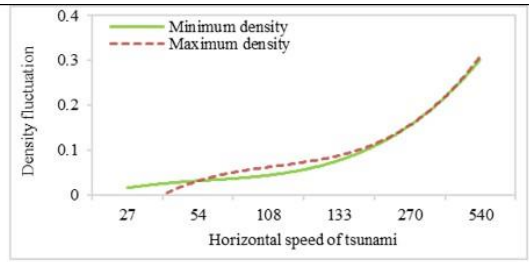
Fig. 2: Density profile for extreme horizontal speed

Here we have not taken damping effects resulting from energy dissipation and the complexities arising from intermediation and nonlinear effects of gravity waves in the atmosphere. These factors have the potential to reduce the amplitudes listed in the Table 1 by making them comparable with marginally detectable experimental observations. For the F-region, the dispersion relation $\omega^2 k_z^2 = (\omega_g^2 - \omega^2)k_z^2$ should be utilized, where ω represents the angular frequency of the wave, k_z is the wave vector component along the z-direction and ω_g refers to the gyrofrequency, which is associated with the Earth's magnetic field. By utilizing this dispersion relation, one can analyze the behavior and propagation of waves in the F-region of the Earth's ionosphere.

A preliminary assessment indicates that disturbances in the F-region will only occur when tsunamis have velocities within the range of 270 to 342 km/h. However, in the nighttime F-region of the equatorial anomalous ionosphere, the perturbations in ionization induced by gravity waves may be amplified through a phenomenon known as spatial resonance. In this scenario, the ionization perturbations caused by gravity waves drift at a velocity that matches the phase velocity of the gravity waves. This gives rise to phenomena such as multiple reflections and the spread of the F-region. It is important to consider these factors when studying the ionospheric effects of tsunamis and their implications on the F-region, taking into account the influence of various mechanisms and phenomena that contribute to the overall behavior of the ionosphere.

B. Instability Analysis in Food Grains, Ethanol, Sugarcane and Sugar

To analyze the instability in food-grains caused by the disruption of the global supply chain due to the COVID-19 pandemic, it is crucial to consider the relationship between the demand for food-grains and the population growth, which currently stands at approximately 80 million per annum. The pandemic has significantly impacted the flow of goods, raw materials, and components, leading to increased prices for food and oil. Consequently, there is a pressing need for research on instability analysis in the food-grains sector. The formula for the world price index for a basket of n items is given by

$$\text{Price index} = \frac{\sum_{i=1}^{n} p_i w_i}{\sum_{i=1}^{n} p_{i0} w_i} \times 100 \tag{3}$$

where p_i, p_{i0}, w_i denote the current price, base period price and weight assigned to the ith item respectively.

World price index (WPI) of a basket of food commodities e.g. cereals, vegetable oils, sugar, meat, dairy products and food as per Source: https://www.tradingeconomics.com/world/ can be represented as shown by Fig. 3.
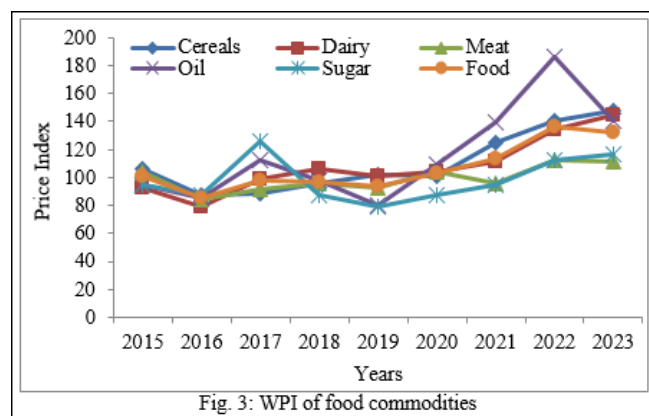

Fig. 3: WPI of food commodities

Food-grains production for the year 2002-03 was estimated at 175 million tonnes and reached a record level of 234 million tonnes in 2008-09. However, it declined to 218 million tonnes in 2009-10. During the pandemic period, there was a significant increase in food-grains production, ranging from 298 to 316 million tonnes, as depicted in Fig. 4a. Due to the increase in the price of average crude oil as shown in Fig. 4b and the record growth production of food grains give us a way to convert food grains into ethanol to mitigate fuel problem.
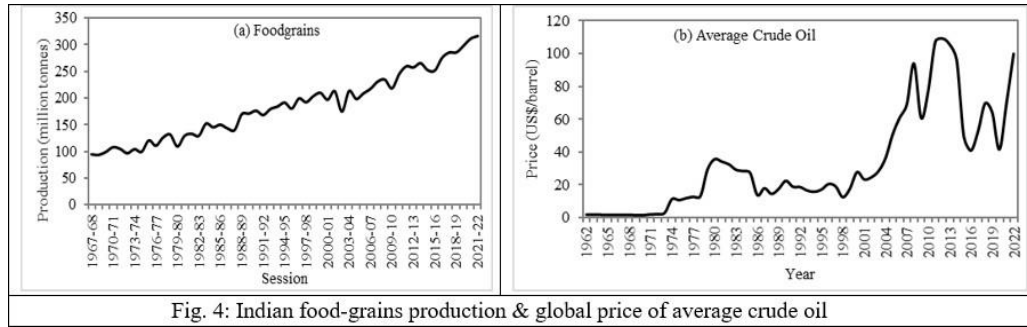
Fig. 4: Indian food-grains production & global price of average crude oil

Consequently, sudden and dramatic increase in energy costs during oil crisis of 1973 paved the way for long-term economic impact for both oil-importing and exporting nations (https://www.statista.com/statistics/262858/change-in-opec-crude-oil-prices-since-1960/). One way to mitigate fuel problem is the blending of ethanol in petrol. Extremely high production and pre-available stock of food-grains during pandemic period has opened a way for the conversion of food-grains into ethanol to mitigate the oil crisis. High oil and ethanol prices affected global economic growth and increased production costs and inflation as shown in Fig. 4b.

The instability in a product can be assessed either by observations or estimated on the basis of Cuddy Della-Valle Index (CDVI), where

$$CDVI = CV \times \sqrt{(1-R^2)}; \; CV = \left(\frac{\sigma}{\bar{X}} \times 100\right)\% \; \& \; \sigma = \sqrt{\frac{\Sigma(X-\bar{X})^2}{n-1}} \qquad (4)$$

Following Sihmar [10], instability can be defined in form of CDVI as follows:
(i) Low instability = 0 - 15   (ii) Medium instability = 15 - 30   (iii) High instability = 30 and above
Applying (4) for instability analysis in Indian ethanol production from 2015-16 to 2021-22, as depicted in Fig. 5a, reveals a high instability with a CDVI value of 57.44.

The Indian government's policies aimed at controlling oil prices have resulted in a decrease in the price of ethanol, while maximizing its productivity through the use of wheat, maize, sugarcane, rice and other crops, as illustrated in Fig. 5a & 5b. The reduction in ethanol prices in India can be attributed solely to the increased production of sugarcane, which plays a significant role in mitigating the oil crisis, as shown in Fig. 5b.

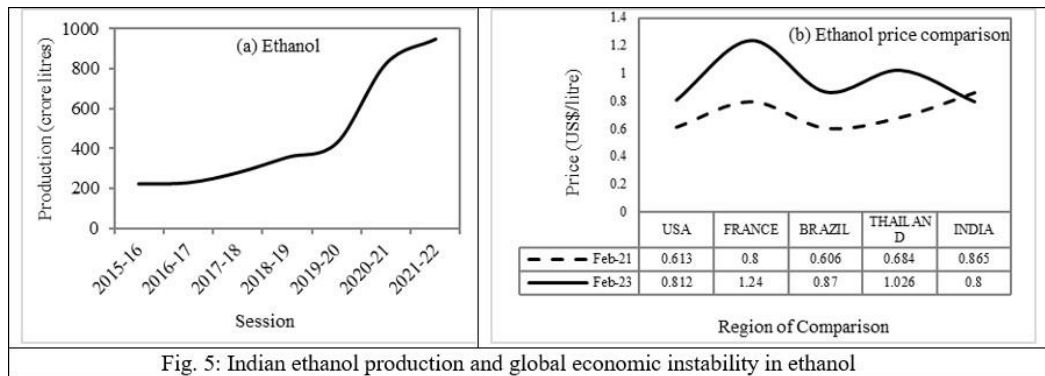|	USA	FRANCE	BRAZIL	THAILAND	INDIA
Feb-21	0.613	0.8	0.606	0.684	0.865
Feb-23	0.812	1.24	0.87	1.026	0.8

Fig. 5: Indian ethanol production and global economic instability in ethanol

Agricultural development plays a crucial role in the overall progress of a nation. In recent years, the high consumption of fossil fuels has prompted the exploration of renewable energy sources. Among these sources, agro-energy crops and plant residues have emerged as highly promising, low-cost, and sustainable biomaterials for biofuels and power generation. In India, sugarcane stands out as a major multi-product cash crop.

Table 2: Extreme values of CDVI for sugarcane in worldwide

Parameter	CDVI (%)	
	Max.	Min.
Area	0.62 (1971-80)	0.17 (1991-00)
Production	0.99 (2011-22)	0.11 (2001-10)
Yield	0.79 (1961-70)	0.33 (1971-80)
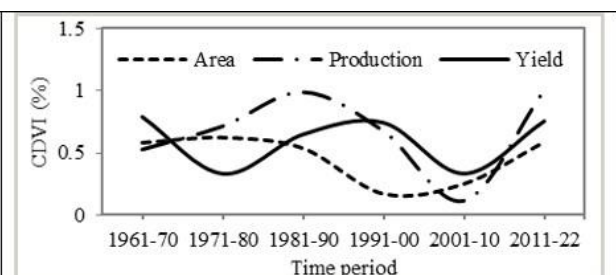
Fig. 6: Instability diagram for sugarcane globally

Source:https://ourworldindata.com

Following Pawan Kumar Sharma *et al* [11] and Agricultural Statistics at a Glance 2022 [12], instability in sugarcane has been analyzed on the basis of CDVI formula given by (4). The computational results for the given parameters of sugarcane in India and globally are given in Table 2 and Fig. 6.

Fig. 6 illustrates the instability behavior of sugarcane based on the given parameters. Additionally, Table 2 showcases the extreme values of the CDVI for different parameters of sugarcane on a global scale.

Table 3: Extreme values of CDVI for sugarcane in India		
Parameter	CDVI (%)	
	Max.	Min.
Area	8.85 (1950-65)	3.57 (1980-95)
Production	12.42 (1950-65)	4.09 (1980-95)
Yield	8.26 (1965-80)	2.42 (1980-95)
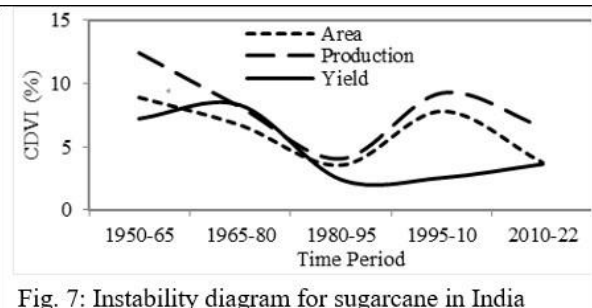
Fig. 7: Instability diagram for sugarcane in India

Source: https://ourworldindata.com

These extreme values indicate low levels of instability for the specific parameters, as observed through the CDVI analysis. Fig. 7 represents the instability behavior of sugarcane for the given parameters and attached Table 3 demonstrates the extreme values of CDVI for various parameters of sugarcane in India which indicates low instability for the selected parameters by CDVI observations. The graphical results show that production of sugarcane exhibits the highest instability among others since 1950 onwards.

Moving on to Fig. 8, it represents the impact of Indian economic instability effect specially caused by the sugar industry. During the period of 2009-10, significant losses were incurred, while there has been a consistent growth in net profit starting from 2017-18 onwards. The reason behind these losses can be attributed to the delayed progress in monsoon, whereas the subsequent years have shown a positive effect on India's economy due to increased net profit in the import-export of sugar, even during the challenging times of the COVID-19 pandemic.
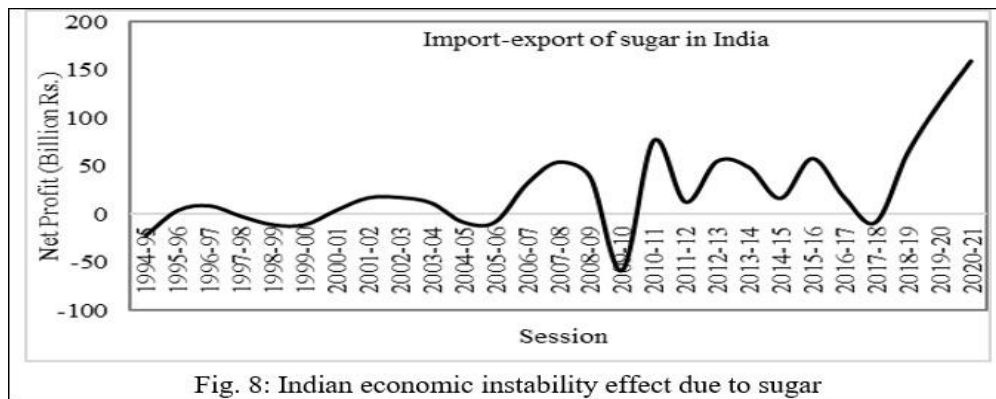

Fig. 8: Indian economic instability effect due to sugar

C. Mitigation of Oil Crisis by Sugarcane, Ethanol and Lithium

Based on the information from the sources provided (https://www.statista.com/statistics/281606/ethanol-production-in-selected-countries/ & https://www.statista.com/statistics/606684/world-production-of-lithium/), sugarcane, ethanol and lithium have been identified as potential remedies for addressing the issue of high oil instability. Sugarcane biomass can be utilized to generate bioelectricity and is currently the fourth-largest source of electricity in the Brazilian energy matrix, contributing approximately 18,400 GWh in 2022. This highlights the significant role of sugarcane in the production of renewable energy. Furthermore, the increasing global production of these products indicates a positive trend towards mitigating oil crises as shown in Fig. 9. By reducing dependence on just-in-time production and international trade, the utilization of sugarcane, ethanol and lithium can help stabilize oil markets. The utilization of Li-ion batteries as alternative energy sources is of utmost importance for both economic stability and sustainable development. The prevailing economic instability has forced researchers to focus on advancing Li-ion battery technology, particularly for the electrification and energy storage needs of the automobile industry. These batteries serve the purpose of storing surplus energy generated during periods of high production and releasing it during times of heightened demand.
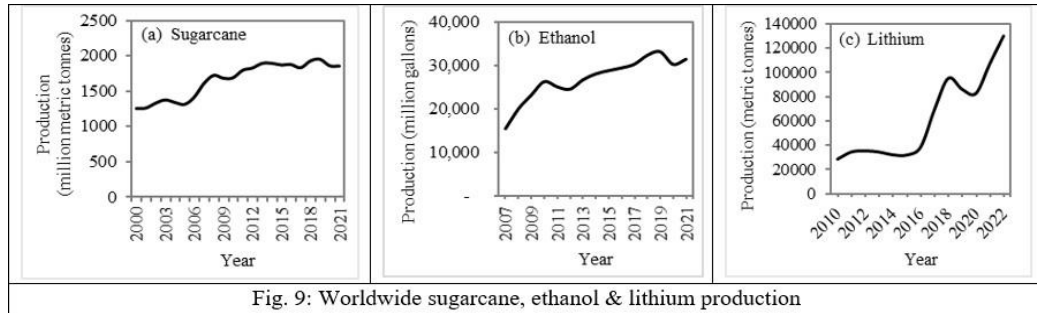
Fig. 9: Worldwide sugarcane, ethanol & lithium production

According to the Geological Survey of India (GSI) and mining authorities, the Degana region in Rajasthan and the Salal-Haiman area of the Reasi district in Jammu & Kashmir possess substantial lithium reserves, capable of fulfilling approximately 80% of India's total lithium demand. This highlights the potential for indigenous lithium sources to contribute significantly to the country's requirements. The average price of Li-ion batteries has witnessed a decline due to several factors, including increased worldwide lithium production, reduced logistics costs, and the scaling up of Li-ion battery manufacturing. This has resulted in a positive trend of cost reduction. As a result, Li-ion batteries have become increasingly suitable for supporting sustainable growth across various industries. However, it is worth noting that the rise in demand for volume-weighted Li-ion batteries and the increase in the average production cost of lithium carbonate have contributed to a 7% increase in the average price of Li-ion batteries in 2022 compared to 2021. This information is illustrated in Fig. 10a & 10b, which likely provide visual representations of the mentioned price trends.
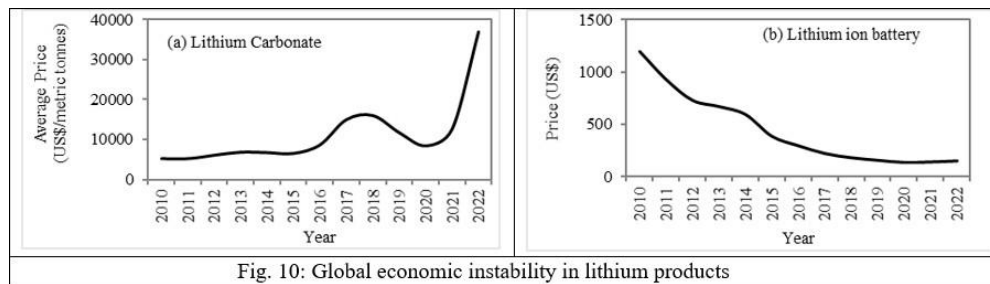

Fig. 10: Global economic instability in lithium products

D. Instability analysis in fluids for horizontal and inclined planes

In 1916, Lord Rayleigh pointed out that onset of instability in a fluid depends upon the value of non-dimensional parameter called Rayleigh Number defined by:

$$\text{Rayleigh Number} = \frac{\text{Buoyant Force}}{\text{Viscous Force}} = \frac{g\alpha\Delta T L^3}{\kappa\nu} \tag{5}$$

Following Kumar & Kaushika [13], Chandrasekhar [14] & Rathy [15], the instability in a system can be analyzed with normal mode technique by converting continuity, momentum and energy equations into non-dimensional form by substituting

$$u = U(y)e^{i(ax+bz)+ct}, \quad v = V(y)e^{i(ax+bz)+ct}, \quad w = W(y)e^{i(ax+bz)+ct}, \quad \bar{T} = \theta(y)e^{i(ax+bz)+ct},$$

$p = \rho_0 P(y)e^{i(ax+bz)+ct}; k(a,0,b)$ is known as wave number & c is the complex wave velocity. The resultant non-dimensional form of equation so obtained is given by

$$(D^2 - h^2)^3 V + h^2 RV = 0 \tag{6}$$

For both the rigid surfaces; let $V_e = A\cos q_0 y + B\cos h\, qy + B\cos h\, \bar{q}y$ and $V_o = A\sin q_0 y + B\sin h\, qy + B\sin h\, \bar{q}y$, are the even and odd solutions of the (6); where A, B are arbitrary constants, q^2 is a root of the equation $(q^2 - h^2)^3 = -Rh^2$ and is given by $q = q_1 + iq_2$ such that

$$q_1 = \frac{h}{\sqrt{2}}\sqrt{\sqrt{(1+n+n^2)}+1} + \frac{n}{2}, q_2 = \frac{h}{\sqrt{2}}\sqrt{\sqrt{(1+n+n^2)}-1} - \frac{n}{2} \ \& \ q_0{}^2 = h^2(n-1) \tag{7}$$

The characteristic equations so obtained for even and odd solutions of (6) are given by

$$im\left[(\sqrt{3}+i)q\tan h\left(\frac{q}{2}\right)\right] + q_0\tan\left(\frac{q_0}{2}\right) = 0 \ \& \ q_0\cot\left(\frac{q_0}{2}\right) = im\left[(\sqrt{3}+i)q\left(\frac{\sin h\, q_1 - i\sin q_2}{\cos h\, q_1 - \cos q_2}\right)\right] \tag{8}$$

As we know that minimum value of Rayleigh number in the graph for the particular value of wave number for odd & even solutions will give the critical Rayleigh number corresponding to the given wave number.

Therefore, solving characteristic (8) by hit and trial method for the applied boundary conditions we obtained critical Rayleigh numbers represented by Table 4 and Fig. 11.

Table 4: Critical Rayleigh number for the fluid heated from below

Shape of boundary	Both open surface	Both rigid surface	One rigid ($y = 0$) and one open surface ($y = 1$)
Boundary conditions	$V = D^2V = (D^2 - h^2)^2V$ $= 0 \; at \; y = 0 \; \& \; 1$	$V = DV = (D^2 - h^2)^2V = 0 \; at \; y = 0 \; \& \; 1$	$V = (D^2 - h^2)^2V = 0 \; at \; y = 0 \; \& \; 1;$ $DV = 0 \; at \; y = 0 \; \& \; D^2V = 0 \; at \; y = 1$
Characteristic equations	$R = \dfrac{(n^2\pi^2 + h^2)^3}{h^2}$	For even solution $im\left[(\sqrt{3} + i)q \tan h\left(\frac{q}{2}\right)\right] + q_0 \tan\left(\frac{q_0}{2}\right) = 0$ For odd solution $q_0 \cot\left(\frac{q_0}{2}\right) = im\left[(\sqrt{3} + i)q\left(\frac{\sin h \; q_1 - i \sin q_2}{\cos h \; q_1 - \cos q_2}\right)\right]$	NA
R_c for h	$R_c = 657.5, h = 2.214$	For even solution $R_c = 1707.76, h = 3.117$ For odd solution $R_c = 17610.39, h = 5.365$	$R_c = 1100.65, h = 2.682$

In conclusion, when observing the graph for a wide range of wave numbers, we have seen that the critical Rayleigh numbers obtained in the even solution are significantly lower than those in the odd solution. This indicates that odd perturbations have a greater adverse effect on the onset of instability compared to even perturbations. It's worth noting that the computed values of the critical Rayleigh number R_c are independent of the Prandtl number P_r of the fluid. Furthermore, these computed values align well with the experimental results of Heitz & Westwater [16] as well as Edward & Catton [17].
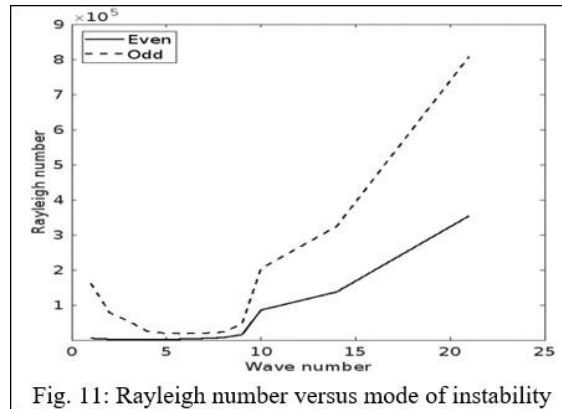

Fig. 11: Rayleigh number versus mode of instability

To study the case of finite prandtl number let us consider heat conservation equation

$$\frac{\partial T_s}{\partial t} = ĸ\frac{\partial^2 T_s}{\partial z^2} \tag{9}$$

$$where \quad T_s = T_0 - \varDelta T\left(\frac{z}{L} - \frac{1}{2}\right) \; such \; that \; T_s = \begin{cases} T_0 - \frac{1}{2}\varDelta T \; at \; v = 0 \; when \; z = L \\ T_0 + \frac{1}{2}\varDelta T \; at \; v = 0 \; when \; z = 0 \end{cases} \tag{10}$$

The resultant non-dimensional steady state equations so obtained are given by

$$\nabla^2\theta = R_a w = v.\nabla\theta \quad \& \quad \nabla^2\theta + \theta\hat{z} - \nabla p = \frac{1}{P_r}q.\nabla q \tag{11}$$

On solving above equations, we get mathematical results as

$$R_a = \begin{cases} 2031 - \dfrac{13.7}{P_r} + \dfrac{24.2}{P_r^2} \; ; for \; two \; dimensional \; rolls \\ 2595 + \dfrac{144}{P_r} + \dfrac{197}{P_r^2} \; ; for \; hexagonal \; cells \end{cases} \tag{12}$$

Following Schluter *et al* [18] and Busse [19], R_a is positive for all cell shapes and motion can occur only if $R_a{}^* = R_c + \varepsilon^2 R_a$.

For slightly large values of the non-dimensional Rayleigh number (R^*_a), there exists a continuum of possible wave numbers. For each wave number, there is a critical Rayleigh number (R_c) below which no motion can occur. As the Rayleigh numbers become larger with smaller Prandtl numbers (P_r), the convective motion becomes unsteady, leading to oscillatory convection or turbulence. Based on Busse's observations, we can identify two types of instabilities for finite small Prandtl numbers. In the case of water, neither of the low Prandtl number instabilities occurs before reaching an infinite Prandtl number, as depicted in Fig. 12a. On the other hand, for air, the Eckhaus type instability occurs before the cross roll type when the difference between Ra and Rc is small, as illustrated in Fig. 12b.
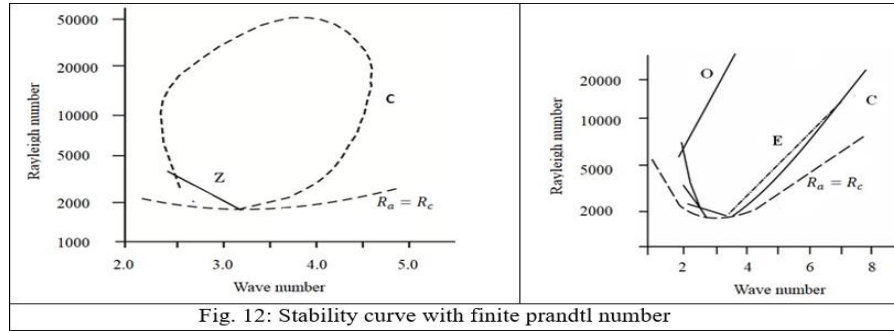
Fig. 12: Stability curve with finite prandtl number

In Fig. 12, the labels C, Z, O, and E represent the cross roll, zigzag, oscillatory and Eckhaus instability curves, respectively. The conclusion drawn from this analysis is that, for a finite Prandtl number and slightly large values of the Rayleigh number in air, the cross roll instability will occur first. Subsequently, for a sufficiently large Rayleigh number, approximately 6000, which aligns closely with the experimental value of 5800, the oscillatory instability will occur.

The case of infinite Prandtl number can be analyzed using the Fourier series expansion for θ & W represented as

$$\theta = \sum_{m=-\infty}^{\infty} \sum_{n=1}^{\infty} b_{mn} \, e^{im\alpha x} \sin n\pi z \qquad \& \qquad W = \sum_{m=-\infty}^{\infty} \sum_{n=1}^{\infty} b_{mn} \, e^{im\alpha x} v_n(m\alpha, z) \quad (13)$$

$$\text{We get } (D^4 - 2m^2\alpha^2 D^2 + m^4\alpha^4)v_n = \sin n\pi z \, ; v_n = 0 \text{ when } z = 0, 1, D = \frac{\partial}{\partial z} \quad (14)$$

This equation can be used to analyze the behavior of the system under the conditions of infinite Prandtl number. Using Boussinesq approximation, the perturbation equations for stability analysis may be taken as

$$\begin{cases} T = \sum_{m=-\infty}^{\infty} \sum_{n=1}^{\infty} C_{mn} e^{im\alpha x} \sin n\pi z \; e^{[i(ax+by)+ct]} \\ V = \sum_{m=-\infty}^{\infty} \sum_{n=1}^{\infty} C_{mn} e^{im\alpha x} v_n(\mu, z) \, e^{[i(ax+by)+ct]} \end{cases} \quad (15)$$

where $\mu = \sqrt{[(m\alpha + a)^2 + b^2]}$.

By linearization with respect to small quantities θ & W we get the characteristic equation in c. For infinite prandtl number & $a = 0$ with high growth rate, we see that the range of stability changes from cross roll instability to zigzag instability when $(m + n)$ changes from odd to even as shown in Fig. 13. This figure shows the marginal stability diagram for fluids with infinite prandtl number. In this diagram curve C represents cross roll instability and curve Z represents zigzag instability.

Fig. 13: Marginal Stability Diagram with infinite Prandtl number

Based on the findings, it can be concluded that:

➢ Critical cross roll instability occurs if h increases from 3.117 (when $R_a = R_c$) to 4.5.
➢ If R_a is extremely large. Two-dimensional rolls become unstable for all wave numbers.
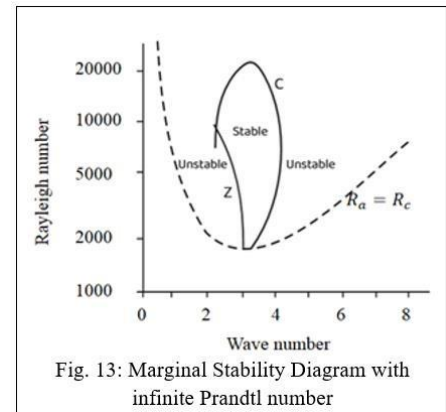➢ The values of b exhibit minimal dependence on the wave number of the original rolls.

The findings reveal a significant correlation between specific parameters and the occurrence of cross roll instability, shedding light on the behavior of the system. In Fig. 14, we observe the development of zigzag instability in the system. Through experimental observation at high Rayleigh numbers, it is evident that rolls remain stable when $R_a < 22600$. However, for low wave numbers, we witness the emergence of zigzag instability. This instability grows over time until the perturbations of neighboring rolls combine to form rolls with a larger wave number, positioned at an angle of 45^0 to the original rolls. This transition typically occurs within a span of 1 or 2 hours. On the other hand, when $R_a > 22600$, the cross-roll instability triggers a steady three-dimensional motion referred to as bimodal convection. Eventually, this bimodal convection becomes unstable, leading to the observation of oscillatory convection. These observations provide valuable insights into the dynamic behavior of the system under different conditions. Based on the experimental and computational results by Krishanamurti [20] for the transition to oscillatory convection when $R_a \approx 2500 P_r$ for oils with Prandtl number lying between 16 and 126, we observed that if critical Rayleigh number increases from 40000 to 50000, the rolls become unstable. It is worth noting that the initial conditions also play a significant role in the transition to time-dependent instabilities. On the basis of rolls, instability in fluids may be classified as shown in Fig. 15. The singly hatched region represents the stability for all prandtl numbers while doubly hatched region represents the stability for small prandtl numbers. For mercury, the rolls are always unstable when the Rayleigh number exceeds 2400, while for air, the rolls become unstable when R_a is greater than 5600. As for water, which is known for its high

Prandtl number, the transition to bimodal convection occurs when $R_a \approx 17000$, and oscillatory convection occurs when $R_a \approx 35000$.

Fig. 14: The Development of Zigzag Instability

Fig. 15: Instability curves
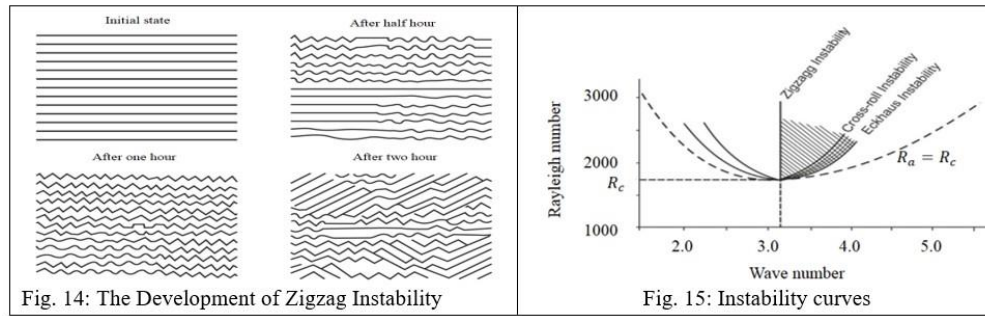
Despite the significant progress made in this field, there is still some unresolved disparity between the experimental results at these higher transitions, and further work is required to gain a better understanding of the behavior of the system under different conditions.

Now, let us consider the case of inclined plane making an angle β with upward vertical. Then following Hart [21] we get a steady state solution to the Boussinesq equations of the form $v_0 = [u(z), 0,0]$, $T_0 = rx + T(z)$; where $u(z), T(z)$ are linear functions of mz cosh mz and cos mz sinh mz, r is an arbitrary constant and $R_a = \frac{4m^4}{r \cos \beta}$. Then taking $A = \frac{L}{d}$ up to 0.04, Hart's experimental observations give that r=0 when $R_a \cos \beta < 10000$, r=0.62 L when $R_a \cos \beta > 52000$ and r=0.87[log($R_a \cos \beta$) − 4]L for the intermediate range of $\beta \geq -70^0$ and $R_a \cos \beta$. The temperature and velocity so obtained have a good agreement with predicted form for $R_a = \frac{4}{r \cos \beta} \left(\frac{m}{1.09}\right)^4$.

Now let perturbation equations are given by $f(z) = e^{-i\omega t} e^{i(ax+by)}$, where $10^0 < \beta \leq 90^0$ and $-85^0 < \beta < -10^0$. Then instability occurs at $b = 0$ & $\omega = 0$ and the convection will set up in the form of steady longitudinal rolls along the lines of greatest slope. Further if $\beta \leq 60^0$ and $A \leq 0.009$, steady transverse shear modes exist. If $|\beta| < 10^0$, the instability will occur for $a = 0$ and $\omega \neq 0$ and is in transverse travelling modes.

Fig. 16 represents the stability diagram for $A = 0.04$ and $P_r = 6.7$ and the longitudinal rolls corresponding to Rayleigh and wave numbers has been represented by Fig. 17. A number of experiments for $A = 0.027$ and 0.04 for water has been performed to determine wave numbers. As a result, transverse travelling waves are predicted at slightly lower Rayleigh numbers than those observed. Further, we get good agreement with theoretical curves except the transverse travelling waves corresponding critical Rayleigh numbers as shown in Fig. 18. Finally, if we consider a fluid layer inclined from horizontal and heated from below, it is never possible for the fluid to be stationary. Since the unbalanced buoyancy force always creates some motion. The flow for which $R_a < \frac{1708}{\cos \beta}$, is called the base flow existence. The motion consists of a single cell with fluid rising from
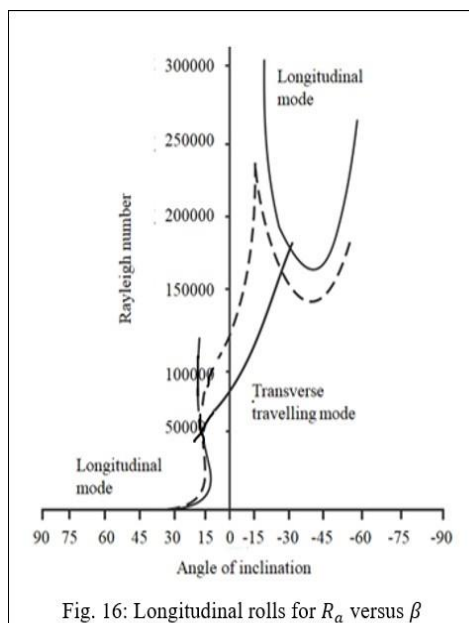

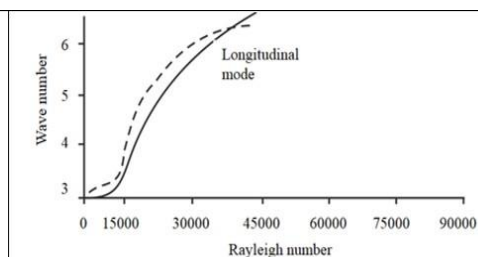Fig. 16: Longitudinal rolls for R_a versus β

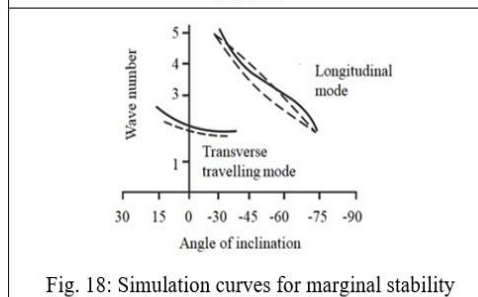Fig. 17: Longitudinal rolls for R_a versus wave Number

Fig. 18: Simulation curves for marginal stability

the hot surface and falling along the cold one and turning at upper and lower extremes of layer. The flow normal to the plates will be the flow of convecting heat across the layer and consequently, in middle region the heat transfer across the layer is only by conduction. In stationary fluid $N_u = 1$, So for $R_a > \frac{1708}{\cos\beta}$, Convective cell set inside which are analogous to those occurring in horizontal layer at $R_a > 1708$, and nusselt number increases. Although for $\beta < 20^0$ they consist of steady rolls with axis along the upslope direction, for $\beta > 20^0$ these rolls quickly breakdown into more complex flow patterns.

E. Instability mitigation in fluid bounded by honeycomb structures

When a cellular matrix (TIM Device) is introduced in the fluid layer maintained between two infinite isothermal bounding surfaces with finite vertical depth, the vertical walls provide extra viscous resistance to the onset of convection and effectively raise the critical Rayleigh number R_c, which depends on physical shape and dimensions of honeycomb cells as well as on the thickness and thermo physical properties of the cell walls. Engineers often cite hexagonal shape of bee honeycomb as most economical use of two-dimensional space. Subsequently, amongst others, circular, square and rectangular cells have also been investigated. Vertical absorber structures are in the most advanced stage of development, it includes honeycombs, capillaries and parallel slat arrays. In vertical absorber structures cell walls are placed perpendicular to absorber plane. The advantage of this configuration is the forward reflection of solar radiation by vertical walls and thus major portion of incident radiation reaches the absorber. The major heat loss made from the absorber is convection, which can be significantly suppressed by proper design of the cell dimensions. Following Smart et al [22] and Cane et al [23], a square celled honeycomb can be designed such that $\left(\frac{R_a}{A^4}\right) < 6000, 30^0 < \beta < 90^0$, for $A \geq 4$, which satisfy the criteria for nusselt number given by $N_u = 1.0 + 0.89 \cos\left(\beta - \frac{\pi}{3}\right)\left(\frac{R_a}{2420\,A^4}\right)^{2.88 - 1.64\sin\beta}$.

The cavity structure is a combination of absorber-parallel and absorber-vertical structures. It includes duct plates and foams. The problem associated with this type is the higher solar optical losses, but the heat losses are suppressed significantly. Homogeneous material includes the TIM of glass fibers and aerogels. These materials can be used for higher temperature.

Table 5: Honeycomb design for instability mitigation

Honeycomb depth L (cm)	Aspect ratio (A=L/d)	U_L	$(\alpha\tau)_{eff}$ (black absorber)
5	10	2.0	0.75
10	20	1.5	0.69
15	30	1.0	0.65

The scattering and absorption are little more in these materials compared to other TIM. Solar transmittance and heat loss coefficient are the two parameters used for their characterization. So, further parametric investigations are needed for sustainable development in green energy development.

The solar collection effectiveness of TIM devices can be judged by an accurate determination of solar transmittance and heat loss coefficient across the devices. Solar beam radiation transmittance and its effect on instability mitigation for these devices has been investigated by several researchers e.g., Hollands et al [24], Arulanantham & Kaushika [25] and Kaushika et al [26]; The formulation of these investigations has been used to derive $(\alpha\tau)_{eff}$ for the design of various types of cellular structures. As a result of computational & experimental observations, we can say that thermal instability in the fluid can be suppressed by a suitable choice of aspect ratio of cellular structure for the selected medium (air/water) for instability mitigation, Overall heat transfer coefficient with respect to aspect ratio for the selected depth of honeycomb have been represented in Table 5.

In favor of practical interest, the range of nusselt number (1 to 1.5) corresponds to almost non convective state of fluid which is very helpful for innovative design of the cellular structures for instability mitigation in solar energy application. Holland considered the base flow and recommended the engineering design of cellular structure with nusselt number 1.2. Therefore, using $N_u = 1.2$ the minimum aspect ratio A that is required just to suppress the convection is given by

$$A = F(\beta)\left(\frac{R_a}{2420}\right)^{\frac{1}{4}}; \quad F(\beta) = (4.45\cos(\beta - 60))^{\frac{1}{(11.52 - 6.56\sin\beta)}}, R_a = 2737(1 + 2\beta_1)^2\beta_1{}^4\Delta T(100L)^3p^2;$$

$$30^0 \leq \beta \leq 90^0, \beta_1 = \frac{100}{T_m}, T_m(in\ K) = \frac{(T_h + T_c)}{2}, \Delta T(in\ K) = T_h - T_c; 280K \leq T_m \leq 500K \quad (16)$$

By analytical observations, we see that the above expression is also valid for β = 0, if F (β) is taken as 1.072 and the linear interpolation of values for the range 0^0 to 30^0 is also permitted. For air, at atmospheric pressure and moderate temperature $(280K \leq T_m \leq 370K)$ the minimum cell width that is required to just suppress the convection is

$$d = \frac{(100L)^{1/4}}{100\,c(\beta)(1 + 2\beta_1)^{1/2}\beta_1(\Delta T)^{1/4}}\,mts = \frac{(100L)^{1/4}}{c(\beta)(1 + 2\beta_1)^{1/2}\beta_1(\Delta T)^{1/4}}\,cm \quad (17)$$

where L is in m, β_1 is in K^{-1}, ΔT is in K. The function $c(\beta)$ is given by
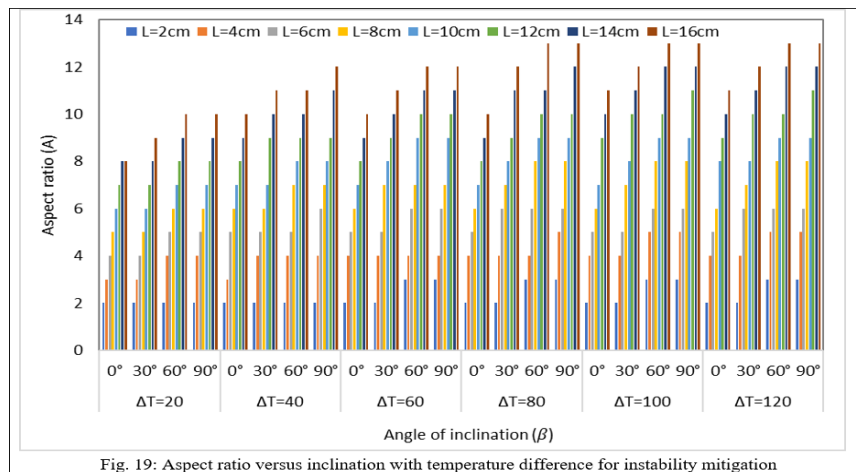
$$c(\beta) = 1.03\,F(\beta) = 1.03\,(4.45\cos(\beta - 60))^{\frac{1}{(11.52 - 6.56\sin\beta)}}, 30^0 \leq \beta \leq 90^0 \quad (18)$$

$$c(\beta) = 1.1 + 0.25\sin\beta, 0^0 \leq \beta \leq 30^0 \quad (19)$$

The calculations have been made corresponding to thin-walled honeycombs and owing to choose to N_u as 1.2 cover near critical Rayleigh regime.

Table 6: Variation in aspect ratio

ΔT	20°				40°				60°				80°				100°				120°			
β \ L	0°	30°	60°	90°	0°	30°	60°	90°	0°	30°	60°	90°	0°	30°	60°	90°	0°	30°	60°	90°	0°	30°	60°	90°
2	2	2	2	2	2	2	2	2	2	2	3	3	2	2	3	3	2	2	3	3	2	2	3	3
4	3	3	4	4	3	4	4	4	4	4	4	4	4	4	4	5	4	4	5	5	4	4	5	5
6	4	4	5	5	5	5	5	6	5	5	6	6	5	6	6	6	5	5	6	6	5	6	6	6
8	5	5	6	6	6	6	7	7	6	7	7	7	6	7	8	8	6	7	8	8	6	7	8	8
10	6	6	7	7	7	7	8	8	7	8	9	9	7	8	9	9	7	8	9	9	8	8	9	9
12	7	7	8	8	8	9	9	9	8	9	10	10	8	9	10	10	9	10	10	11	9	10	10	11
14	8	8	9	9	9	10	10	11	9	10	11	11	9	11	11	12	10	11	12	12	10	11	12	12
16	8	9	10	10	10	11	11	12	10	11	12	12	10	12	13	13	11	12	13	13	11	12	13	13

Fig. 19: Aspect ratio versus inclination with temperature difference for instability mitigation

The computational results based on the above correlations for honeycomb cell depth in the range of 2 to 16 cm and ΔT in the range of 20^0C to 120^0C gives that cell width range of 7 mm to 19 mm & aspect ratio range of 2 to 13 are sufficient to suppress the convection for various angle of inclination as shown in Fig. 19.

Table 7: TIM optimization for various β & ΔT

L(cm)	Aspect ratio (A)			Width (d) (mm)		
	Min. A	Max. A	ΔA	Min. d	Max. d	Δd
2	2	3	1	7.2	11.4	4.2
4	3	5	2	8.5	13.6	5.1
6	4	6	2	9.4	15.0	5.6
8	5	8	3	10.1	16.1	6.0
10	6	9	3	10.7	17.1	6.4
12	7	11	4	11.2	17.8	6.6
14	8	12	4	11.7	18.5	6.8
16	8	13	5	12.1	19.2	7.1

II. CONCLUSION

By enhancing the efficiency of sugarcane and foodgrains, a country can augment its revenue by means of exports or the utilization of their by-products. The volatility in oil and ethanol prices has had a negative impact on economic progress and has led to increased production costs and inflation. As a result, we are exploring alternative fuels derived from sustainable bio resources. This focus on energy innovation has laid the groundwork for the renewable energy sector. Consequently, the blending of ethanol in petrol and the widespread adoption of Li-ion batteries play a crucial role in the economic and sustainable development of the world. The study of economic instability has compelled researchers to advance Li-ion battery technology for the electrification and energy storage needs of the automotive industry. On the other hand, computational investigations conducted on the fluid layer without a Prandtl number have revealed interesting findings. It has been observed that odd perturbations have a more detrimental effect on the onset of instability compared to even perturbations, particularly in the case of horizontal planes. The critical Rayleigh number obtained from even perturbations aligns well with the experimental results of Heitz and Westwater, validating the accuracy of the computational study. At higher Rayleigh numbers and lower Prandtl numbers, the convective motion exhibits unsteady behavior, characterized by oscillatory convection or turbulence. Additionally, the research highlights the significant role of aspect ratio in suppressing instability in honeycomb designs. These findings contribute to a deeper understanding of fluid instability phenomena and offer insights for future research in this field.

REFERENCES

[1] A. S. Arya, "Reconstruction after tsunami pro managing safety challenges ahead (edited by Pradeep Chaturvedi)," Concept Publishing Company, 2004.

[2] A. V. Koustov, K. Schlegel, "Internal Gravity Waves in the Earth's Atmosphere", Journal of Geophysical Research, 1999.

[3] T. Fukushima, Y. Mori, T. Yasuda, "Tsunami Simulation with a Fully Nonlinear Boussinesq Model," Journal of Fluid Mechanics, 2007.

[4] J. N. Moum, J. Nash, "Internal Waves and Ocean Mixing," Annual Review of Fluid Mechanics, 2009.

[5] C. E. Synolakis, "Tsunami run up on street slopes," Hazards 4, pp. 221-234, 1991.

[6] C. E. Synolakis, E. J. Skgelbreia, "The four zones in the evolution of solitary waves on plane beaches," Journal of Waterways Ponds and Coastal Engineering, ASCE vol. 118(3), pp. 252-266, 1993.

[7] N. D. Kaushika, LAFE – 185 PR "Conselho Nacional de per Quisas," S J Compaos Brazil, 1972.

[8] N. D. Kaushika, E O S, Trans. American Geophysical Union vol. 54(4), pp. 66, 1973.

[9] C. O. Huies, "Internal atmospheric gravity waves," Canadian Journal of Physics, vol. 38, pp. 1441, 1960.

[10] R. Sihmar, "Growth and instability in agricultural production in Haryana: A district level analysis," Int J Sci Res, vol. 4(7), 2014.

[11] P. K. Sharma, S. Gupta, A. Baliyan, M. B. Sharma, "Economic analysis of sugarcane and its by-products for sustainability," Int Res J Management Sci Tech, vol. 14, pp.38-52, 2023.

[12] "Agricultural statistics at a glance 2022" & visit us at http://desagri.gov.in, 22 August 2023.

[13] P. Kumar, N. D. Kaushika, "Convective effects in air layer bounded by cellular honeycomb arrays," J Sci Ind Res, vol. 64, pp. 602- 12, 2005.

[14] S. Chandrasekhar, "Hydrodynamic and hydromagnetic instability", Oxford Clarandan Press, pp. 9-25, 1961.

[15] R. K. Rathy, "An introduction to Fluid Dynamics", Oxford and I.B.H. Publishing Co. Pvt. Ltd., 1976.

[16] W. L. Heitz, J. W. Westwater, "Critical Rayleigh numbers of natural convection of water confined in square cells with l/d from 0.5 to 8," Trans ASME J Heat Mass Transfer, vol. 93, pp. 111-96, 1971.

[17] Edwards D K & Catton I, Prediction of heat transfer by natural convection in closed cylinders heated from below, Int J Heat Mass Transfer, vol. 12, pp. 12-23, 1969.

[18] A. Schluter, D. Lortz, F. H. Busse, Journal of Fluid Mechanics, vol. 23, pp. 129-44, 1965.

[19] F. H. Busse, J Math Phys, vol. 46, pp. 140-50, 1967b.

[20] R. Krishnamurti, J Fluid Mech, vol. 42, pp. 295-07, 1970.

[21] Hart J E, J Fluid Mech vol. 47, pp. 547-76, 1971.

[22] D. R. Smart, K.G.T. Hollands, G. D. Raithby, "Free convention heat transfer across rectangular celled, diathermous honeycomb," Trans ASME J Heat Mass Transfer, vol. 102, pp. 75-80, 1980.

[23] R. L. D. Cane, K. G. T. Hollands, G. D. Raithby, T. E. Unny, "Free convection heat transfer across inclined honeycomb panels," Trans ASME J Heat Mass Transfer, vol. 99, pp. 86-91, 1977.

[24] K. G. T. Hollands, K. N. Marshall, R. L. Wedel, "An approximate equation for predicting the solar transmittance of transparent honeycomb," Solar Energy, vol. 21, pp. 231, 1978.

[25] M. Arulanantham, N. D. Kaushika, "Global radiation transmittance of transparent insulation materials," Solar Energy, vol. 53, pp. 323-08, 1994.

[26] N. D. Kaushika, P. K. Sharma, R. P. Priya, "Solar Thermal Analysis of Honeycomb Roof Cover System for Energy Conservation in an air- conditioned building," Energy and Buildings, vol. 18, pp. 45-49, 1992.